REFERENCE COPY

NATIONAL AERONAUTICS AND SPACE ADMINISTRATION

Technical Report 32-1552

Stress Analysis and Design of Silicon Solar Cell Arrays and Related Material Properties

A. M. Salama
W. M. Rowe
R. K. Yasui

JET PROPULSION LABORATORY
CALIFORNIA INSTITUTE OF TECHNOLOGY
PASADENA, CALIFORNIA

March 1, 1972

Prepared Under Contract No. NAS 7-100
National Aeronautics and Space Administration

Preface

The work described in this report was performed by the Engineering Mechanics and Guidance and Control Divisions of the Jet Propulsion Laboratory.

Acknowledgement

The silicon materials used in this work were provided by K. Ling and P. Iles of Centralab, a division of Globe-Union, Inc., and E. Ralph of Heliotek, a division of Textron, Inc. The thermal expansion measurements described herein were performed by M. D. Campbell of Convair, a division of General Dynamics.

Contents

I. Summary 1

II. Background 2

III. Method of Analysis 3

IV. Thermal Stresses in Interconnectors 4

A. Assumptions and Justifications 4

B. Structural Model 6

C. Failure Prediction 6

D. Material Selection 8

V. Pull Test Correlation with Analysis 10

A. Description of Pull Test 10

B. Analysis of Pull Test 10

C. Results 11

D. Effect of Geometry on Contact Strength 15

VI. Material Properties 16

A. Flexural Testing of Silicon Solar Cell Wafers 16

B. Thermal Expansion Tests on Silicon and Silicone Rubber Adhesives 16

C. Discussion of Test Results 19

VII. Conclusions and Direction of Future Work 22

A. Conclusions 22

B. Recommendations for Future Work 23

References 23

Appendix A. Procedures for Three-Point Flexure Tests and Calculation of Mechanical Properties 25

Appendix B. Test Procedures for Linear Thermal Expansion Tests 27

Appendix C. Micro-VCM Outgassing Data on Polymeric Materials 28

Tables

1. Material properties used for Kovar, solder, and silicon 6
2. Comparison of maximum effective stress for seven groups of candidate materials 10

Contents (contd)

Tables (contd)

3. Results of three-point bend tests on Heliotek solar cell wafers 17
4. Results of three-point bend tests on Centralab solar cell wafers 18
5. Specimens tested for linear thermal expansion 19
6. Outgassing properties of candidate adhesives for solar cell/substrate and solar cell/cover glass bonds 22

Figures

1. Typical cross section of four types of composite arrangements 2
2. An array of solar cells 5
3. Reference system for bay BC 7
4. Finite element model of half bay BC 7
5. Displacements and stresses at a typical node 8
6. Effective stress contours for example of thermal stresses in interconnectors 9
7. Solar cell ohmic contact strength test tab 11
8. Contact strength test configuration 12
9. Typical solar cell with contact strength tab soldered 12
10. Solar cell mounted in materials testing machine prior to contact strength test 12
11. N-contact strength of solar cells as a function of temperature 12
12. Finite element model of contact strength test configuration 13
13. Stress contours in pull test configuration 14
14. Effect of geometry changes on contact strength 15
15. Thermal expansion of solar cell silicon and fused silica cover glass 20
16. Thermal expansion of solar cell/cover glass and solar cell/substrate silicone rubber adhesives 20
17. Scanning electron microscope photographs of edges of Centralab and Heliotek silicon solar cell wafers (×240) 21

Abstract

Mechanical failures that may arise in components of composite solar cell arrays in a thermal environment can be avoided by properly selecting compatible material for the components and introducing certain geometric changes in a proposed design. This report provides the solar cell array designer with a rational systematic approach. A prerequisite to this approach is the characterization of material properties at different temperatures. Significant data was obtained for the thermal behavior of the silicon solar cell material and adhesives. Upon determining the mechanical and thermal material properties of the components of the solar cell array, utilizing a finite element idealization for predicting the stress fields in the components, and employing the von Mises failure criterion, potential failure areas in various design configurations in a given thermal environment can be identified. Guide lines and means to optimize a given design are illustrated by two examples.

Stress Analysis and Design of Silicon Solar Cell Arrays and Related Material Properties

I. Summary

A solar cell array is usually subjected to severe thermal environment while performing its primary function as a power source. Such environments induce stresses in the various components of the array. When the stresses exceed certain limits, mechanical failure can take place in the components, resulting in degradation of the power output of the array. To avoid these failures, the designer must properly select compatible materials for the components. In addition, he may have to modify the design configuration so that the induced stresses do not exceed the failure limits.

The objective of this report is to describe a rational approach that enables the solar array designer to efficiently arrive at the proper design. This objective is accomplished by:

(1) Determining the basic material properties of various components (modulus of elasticity E, Poisson's ratio ν, coefficient of thermal expansion α, and the limiting stress at failure σ^*) at different temperatures (-200 to $+200°C$).

(2) Utilizing a finite element idealization for the prediction of the stress fields in the components of a given design in a given thermal environment.

(3) With the knowledge of the materials characteristics at different temperature and the predicted stresses, a reliable failure criterion is used to determine potential failure areas in the design.

Guidelines and means to select materials and improve a particular design are discussed in connection with two examples (typical *Mariner* 67 bus bar to cell connections in a thermal environment and pull test configuration under mechanical loading).

Although property determination for materials of interest was not completed, significant data was obtained for the thermal behavior of the silicon solar cell material and the dimethyl and phenylmethyl silicone materials. These latter materials are used as adhesives for solar cell to substrate and cover glass to solar cell bonding.

Additional material property determination and further extensions of the analysis procedure are in progress. The work included in this report, however, is particularly significant in that it provides the solar cell designer with a versatile rational approach that eliminates much of the guessing on the designer's part. Accordingly, questions regarding selection among material candidates, materials compatibility, and changes in design configuration can be answered systematically and efficiently.

II. Background

For the last 13 years, solar cell arrays have been designed and placed in space and used primarily as power sources. During their lifetime, and depending on their mission, they may be subjected to severe thermal and mechanical environment. Being an integral part of the solar array, a typical solar cell and its interconnects share thermal and mechanical loads along with other components of the array. Further complications arise from the fact that there are several materials involved in the design of a typical composite solar array. Each material has its own thermal and mechanical properties. For example, as Fig. 1 shows, the solar cell composite is typically made of several layers that include a cover glass, the silicon cell, and adhesive layers to bond the cover glass to the cell and the cell to the substrate. The substrate may, in turn, be made of a honeycomb core sandwiched between two aluminum sheets (skin) with adhesive layers to bond the skin to the core. Finally, the cells are connected together in some fashion with conducting wires (commonly referred to as interconnects or busbars, such as plated Kovar, which are usually soldered to the cells.

When such a composite is subjected to a thermal or mechanical environment, stresses are set up in the different components just mentioned. The magnitude of the stresses in each component depends upon several factors that interact together in a rather complicated way. These factors can result from:

(1) The geometry of each component of the composite and the manner by which these components interrelate with one another,

(2) The type of loading, thermal or mechanical, and the manner of load application,

(3) The temperature-dependent mechanical and thermal material properties such as the modulus of elasticity E, Poisson's ratio ν, and the coefficient of thermal expansion α of each component.

Depending upon the material properties and stressing history of a particular component, when the stresses exceed certain limits, some components will fail mechanically. This will in turn result in degradation of the power output of the array. Thus, in addition to their primary

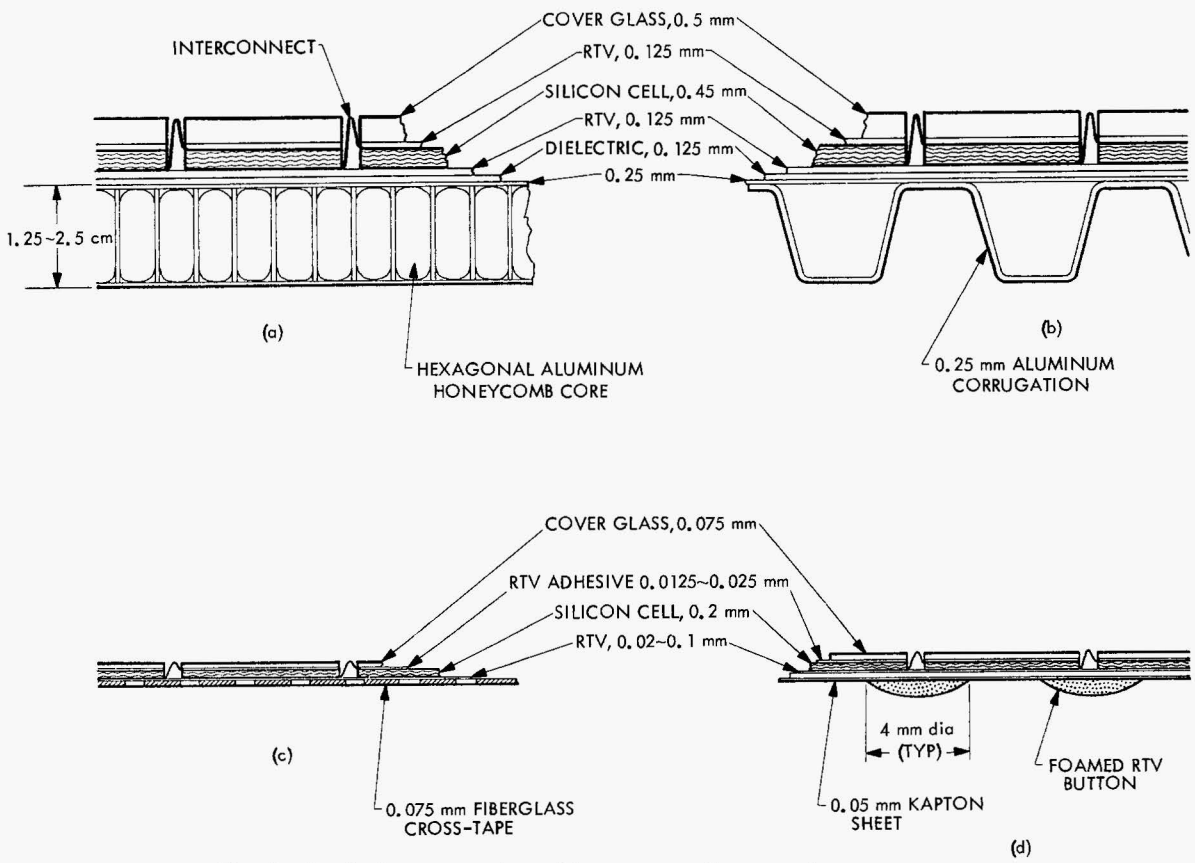

Fig. 1. Typical cross section of four types of composite arrangements

function as power sources, a proper design should ensure the ability of solar cell array components to endure the induced stresses without failure.

In the past few years, efforts have been made to deal with explanations and corrective means to avoid these failures (Refs. 1–5). Some of these earlier attempts were based on empirical tests which frequently lacked sound reasoning and relevance to the real problem at hand. Others used sound analytical methods that were successfully applied to simplified designs but, as expected, fell short of being easily applied to design configurations closely simulating actual designs.

Earlier efforts at JPL included stress analysis of individual components of solar cell arrays where the net strain approach was utilized (Ref. 4). Subsequent work (Ref. 5) made certain improvements in that approach by taking into account shear stresses in the adhesive layers. Also, this latter work included treatments of mechanical loadings on the solar array as well as stress analysis of the stress relief loops between two successive rows of cells. Perhaps the primary obstacle limiting the scope of previous efforts is the very limited and sporadic information about the thermal and mechanical properties of materials used in solar cell arrays. This is especially true for properties at elevated and low temperatures.

With the expectation that future missions such as *Viking* will expose the solar arrays to a much higher number of thermal cycles and even larger thermal variations than those experienced in previous missions, it becomes clear that the need for a reliable method for failure prediction is indeed acute.

This report complements the preceding efforts by describing a generalized analysis and failure prediction procedure which is directly applicable to solar cell design. It also gives the results of material property measurements completed to date. With the help of a better analytical tool and reliable material property characterization, the solar cell designer can choose among the material candidates more efficiently and at less cost and introduce the proper geometric changes so that his final design can successfully survive mission environment.

III. Method of Analysis

The variety of materials and design configurations involved in a typical solar cell array makes it practically impossible to carry out a failure analysis of the array's components by a simplified closed form analytical means. In view of this fact, the designer must rely on a numerical technique. The numerical method described here employs approximations in describing the physical model of solar cell arrays and is commonly referred to as the finite element method. It has been developed and used by structural engineers during the last decade to solve structural problems of various levels of complexity.

In an elastic or inelastic body of material, there is an infinite number of interconnection points between the material particles. It is this fact that makes it difficult to mathematically solve a relatively complex structural problem without some form of approximation. This difficulty can be overcome, however, by assuming that the real body of continuous material is physically subdivided into a finite number of material elements of finite sizes. These elements are assumed interconnected at only a finite number of points (nodes). In this sense, each finite element is regarded as a true continuum having the material properties of the original body of material, while the new assembly of all the elements is regarded as a discretized continuum. This form of idealization allows the description of the resulting model in terms of quantities referring to the node points. For example, when subjecting the body of material to loads, the description of the pattern of deformation and the resulting stress distribution would be in terms of displacement degrees of freedom allowed at the nodes and of the resulting stresses and strains at the nodes. In the limit, as the number of nodes are increased to their original infinite number, the model should tend to exactly duplicate the original body of material. For structural analysis purposes, however, one needs only a small number of these nodes to describe the problem at hand, and there are means to guide the analyst in this respect. How the finite element method proceeds from the concepts just described until the stresses are evaluated has been the subject of several papers in the past few years. More details can be found in Ref. 6.

There are several general computer programs available that use the finite element concept for the analysis of structural components. ELAS, SAMIS, and NASTRAN (Refs. 7–9) are representative of these programs. (The acronyms stand for ELASticity, Structural Analysis and Matrix Interpretive System, and NASA Structural Analysis.) Several versions of these programs, suitable for various computer systems, can be obtained from the Computer Software Management and Information Center (COSMIC), the NASA agency for the distribution of computer programs.

ELAS is a general-purpose computer program which can handle equilibrium problems of linear elastic structures of one-, two-, or three-dimensional continuum. It was used during the course of this study because it provides the user with a broad selection of element types for modeling components. It also has the capability of temperature loading, a feature which is essential for solar array analysis. The application of the program to model and solve problems related to solar arrays is illustrated by the examples in Sections IV and V. For completeness, however, the following paragraph describes some preliminary information about the program.

It is up to the analyst to model his structure in a manner that duplicates the real situation as closely as possible. This involves dividing the original structure into a number of finite elements with finite sizes connected together at a finite number of nodes. Depending on the nature of the problem, the finite elements may be selected from different types that suit different structural components. Assuming now that the analyst has already decided upon a model, the program requires as inputs the geometry of the structure, the material properties, the loading characteristics, and a list of the prescribed geometric boundary conditions.

The geometry will be specified when every node point is given a number (node number) and every node number is assigned a set of coordinates x, y, z in an overall coordinate system X, Y, Z. Also, every element must be assigned an element number, and a list of all element numbers and the nodes they connect must be provided. Depending on the type of element used in the model, every node point will have a certain number of degrees of freedom. These degrees of freedom can be displacements along the directions of the reference coordinate axes X, Y, Z and rotations about these axes.

The material properties of the elements must be specified. All elements may have the same material properties, or every one may have its own distinct properties provided that the total number of elements with distinct properties is not more than 99 (the present program limitation). The material properties for a given element include the modulus of elasticity E, Poisson's ratio ν, and the coefficient of thermal expansion α.

The loading may be prescribed as a uniform pressure, as concentrated loads at the node points, or as sets of temperature changes and temperature gradients in the X, Y, and Z directions. Inertia loading may also be specified. Furthermore, one may have any combination of these loading conditions.

The geometric boundary conditions inform the program as to how the structure is held externally. This usually involves the specification of values of known displacement and/or rotation quantities at the node points (degrees of freedom).

With this information regarding geometry, material properties, loading, and boundary conditions, a particular problem would be completely specified. The computer program proceeds to compute the unknowns, which are the unspecified degrees of freedom at the nodes. These are then used to compute the strains and stresses at the nodes. The displacements/rotations and components of stresses at the nodes are the output of the program.

The advantages of the finite element approach stem primarily from the fact that it can be used to analyze structural components with almost any geometric configuration and boundary conditions. Because solar cell array geometric and thermal loading is usually rather complex, the use of finite elements as an analysis procedure seems very promising. The modeling of a given geometry, however, is up to the analyst. Different geometric configurations require the construction of different models. For the model to reasonably duplicate the actual situation, both skill and care must be exercised.

Like other numerical methods of analysis, the basic approximations inherent in the finite element approach result in approximate values for the stresses. However, the approximation is usually acceptable.

A more refined model typically involves the inclusion of more details of the component geometric configuration and material properties as well as allowing more degrees of freedom. This requires more computer time and memory storage. The analyst must, therefore, compromise between the computer limitations and the degree of sophistication of his model.

IV. Thermal Stresses in Interconnectors

A. Assumptions and Justifications

In this example, attention is centered on illustrating the method, showing how the program can be used to evaluate the strength of a given joint, and showing how it can point our means to improve the design. Figure 2 shows

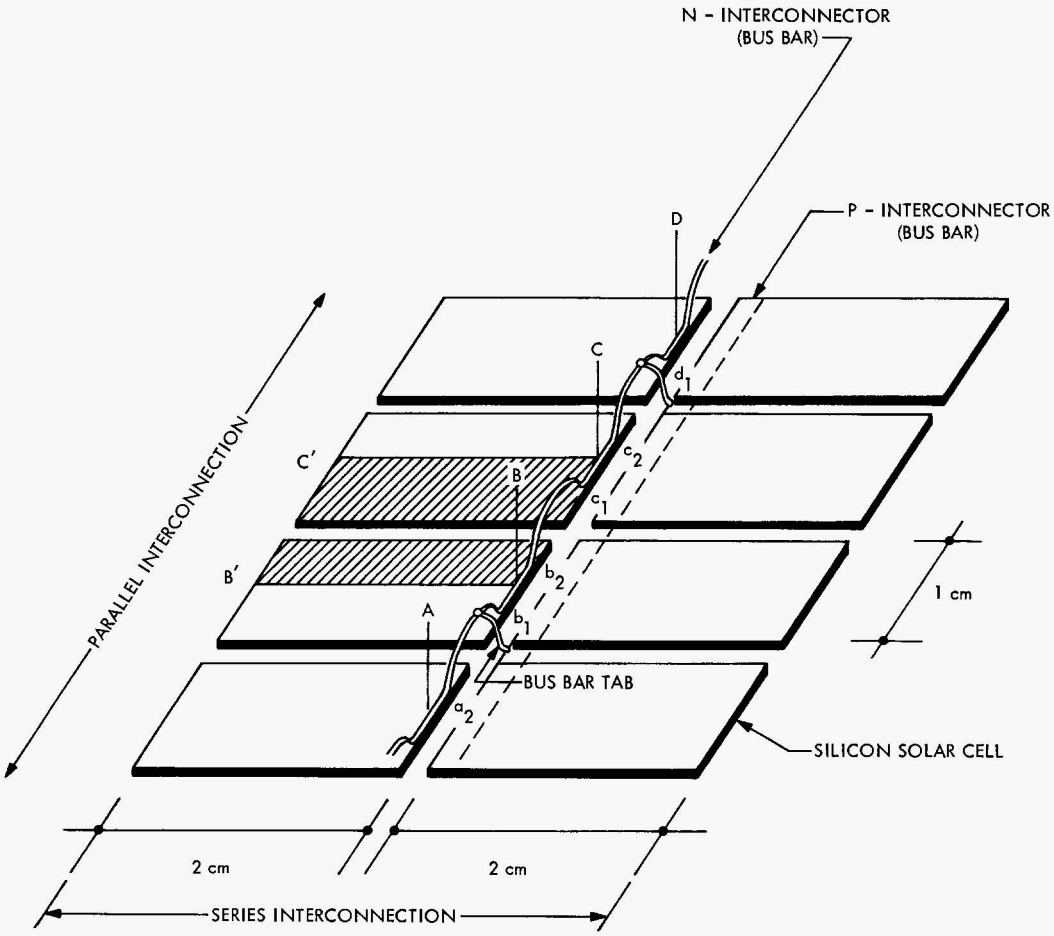

Fig. 2. An array of solar cells

a typical arrangement of solar cells selected for use on the *Mariner* 67 solar cell array design. In this arrangement, an iron–nickel–cobalt alloy (Kovar) bus bar runs across the top side of one row of cells (N-interconnector), and another bus bar connects the lower side of the second row of cells (P-interconnector). The two bars are connected together at intervals with bus bar tabs.

Consider bay BC (shaded area) of the cell/interconnect portion of the array and assume that:

(1) The cell is made of one material whose properties are those of single-crystal silicon.

(2) The cell is rigidly held to the substrate.

(3) All material properties remain unchanged during a temperature change Δt.

(4) Under thermal loading, the displacement and stress fields in bay BC are unaffected by the presence of the tabs in the neighboring bays AB and CD.

(5) The connecting bus bar is tin plated Kovar which is joined to the cell by a conventional eutectic solder alloy (62 Sn/36 Pb/2 Ag).

Of the five assumptions, all but the last deserve further explanation. The first, second, and third assumptions were dictated by the fact that material properties E, ν, α for the cover glass, cover glass to cell adhesive, and cell to substrate adhesive were not available at the time of analysis. In addition, properties for most of the remaining materials existed for room temperature only. The effect of the three assumptions is, therefore, to ignore these materials in an arbitrary manner. These assumptions may not necessarily be conservative, but they are adequate for the purpose of this example.

The fourth assumption is legitimate insofar as bay BC is concerned, but it is not valid for bays such as AB and CD. Because of additional twisting moments and shear forces (resulting from the tab) that exist in bays such as AB and CD, these bays are subjected to a more severe

state of stress than bays such as bay BC. The former are in a three-dimensional state of stress, while the latter are in a two-dimensional state. Therefore, the designer who is interested in the structural integrity of the entire array should consider for his analysis bays of types AB and CD. However, because the present work was limited to one- and two-dimensional stress states, and since this example was chosen to illustrate certain features and usages of the method that equally exist in either a two- or three-dimensional state, bays of type BC are emphasized here.

B. Structural Model

The Kovar bus bar–solder–cell connection of type BC is shown in Fig. 3, with the overall X, Y, and Z reference axes. Taking advantage of the symmetry with respect to the YZ plane, it is sufficient to model only half the connection as shown in Fig. 4.

According to the finite element method description in Section III, the connection shown in Fig. 4 is discretized into a total of 171 finite elements connecting 207 nodes. Of the 171 elements, 66 elements describe the Kovar bus bar, 41 elements describe the solder, and 64 elements describe the cell. These elements are chosen as either triangular or quadrilateral in shape. Unless geometry dictates otherwise, a quadrilateral element is preferred over a triangular one, mainly for efficiency and accuracy of the computations of stresses.

Table 1. Material properties used for Kovar, solder, and silicon (Nominal average values at room temperature)

Property	Kovar	Solder	Silicon
Coefficient of thermal expansion α, cm/cm/°C	(1) 5×10^{-6}	(1) 24×10^{-6}	(3) 2.9×10^{-6}
Poisson's ratio ν	(2) 0.3	(2) 0.3	(2) 0.3
Modulus of elasticity E, N/cm² (psi)	(2) 13.098×10^6 (19×10^6)	(2) 4.136×10^6 (6×10^6)	(3) 6.894×10^6 (10×10^6)
Ultimate failure stress σ_r* N/cm² (psi)	(1) 53,400 (77,500)	(2) 6894 (10,000)	(3) 20,700 (30,000)
Yield stress σ_{yield} N/cm² (psi)	(1) 41,000 (59,500)	(2) 5170 (7500)	(3) 16,540 (24,000)

(1) Westinghouse technical data sheets.

(2) Assumed by interpolating between properties of constituents.

(3) Section VI of this report.

In this two-dimensional model, each node point has two displacement degrees of freedom. Thus, a typical node i can displace in the X direction and the Y direction by an amount u_{ix} and u_{iy}, respectively (Fig. 4). A displacement u_{iz} in the Z direction is irrelevant to a two-dimensional problem. Thus, out of 414 possible degrees of freedom (two at each of 207 nodes), 48 are known to be zero (according to the second assumption and also because of the symmetry of deformation in the model), thus reducing the unknown degrees of freedom to 366.

In this example, an 80°C temperature drop (from +40 to −40°C) with no temperature gradient was assumed. The average material properties used for this temperature range are those of Table 1. With this information, the computed results included:

(1) The set of displacement components, u_{ix}, u_{iy} (Fig. 5a) in the X and Y directions at each node i, ($i = 1, \ldots, 207$).

(2) The set of resulting normal and shear stress components σ_{ix}, σ_{iy}, τ_{ixy} (Fig. 5b) at each node i, ($i = 1, \ldots, 207$).

C. Failure Prediction

The individual values of the set of displacement components u_{ix}, u_{iy} help the solar cell designer mainly in inspecting the results visually. In terms of failure prediction, the more meaningful quantities are the stress components σ_{ix}, σ_{iy}, τ_{ixy}. One of the most widely accepted theories which relate the computed stress components σ_{ix}, σ_{iy}, τ_{ixy} to the failure stress σ^* measured in a simple laboratory test is the von Mises failure criterion.

According to the von Mises criterion, failure at a point in a stressed body takes place when an invariant stress quantity σ_{eff} (effective stress) reaches the corresponding invariant effective stress at failure σ^*, measured in a pure shear or uniaxial tension/compression test[1].

[1]In a one-dimensional state of stress where only one stress component exists (say, $\sigma_x \neq 0$, $\sigma_y = \tau_{xy} = 0$), the invariant effective stress equals in magnitude the nonvanishing stress; i.e., $\sigma_{eff} = \sigma_x$. This follows from Eq. (1).

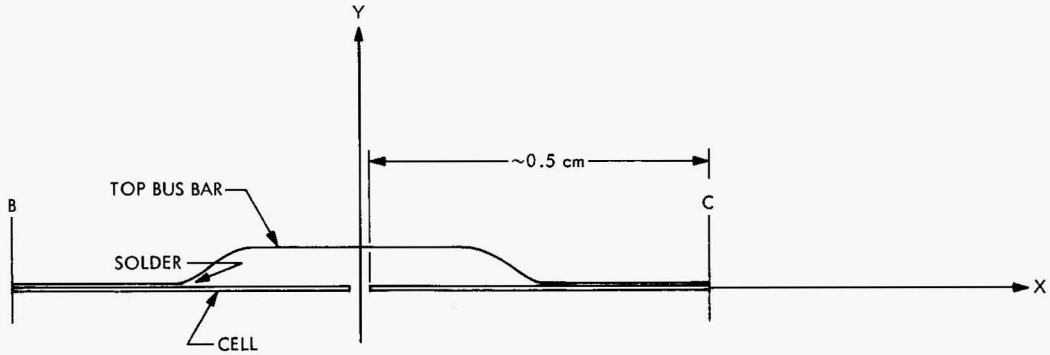

Fig. 3. Reference system for bay BC

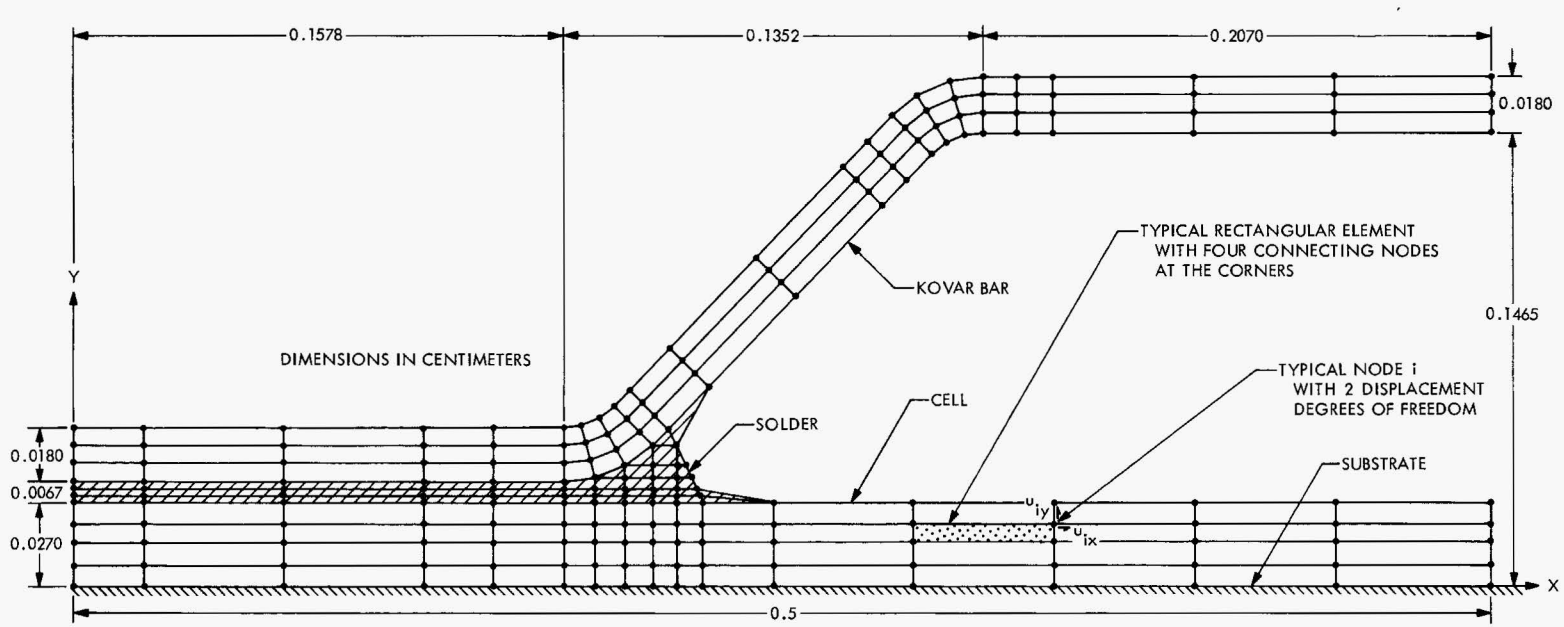

Fig. 4. Finite element model of half bay BC

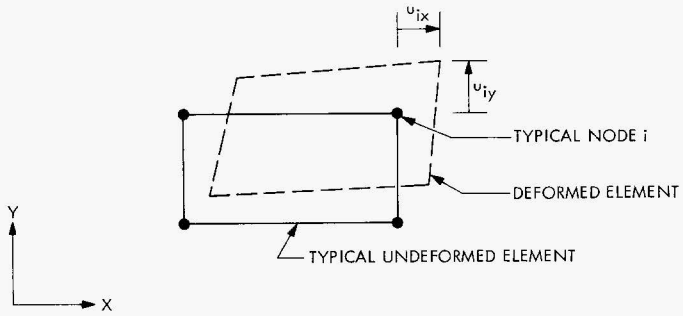

(a) DISPLACEMENT COMPONENTS (u_{ix}, u_{iy}) AT A TYPICAL NODE i.

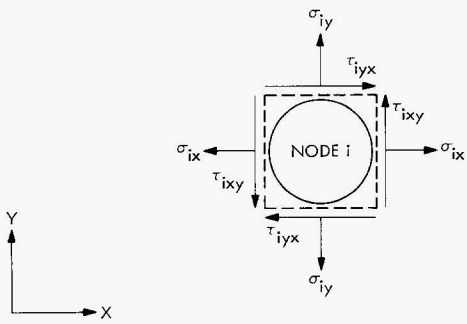

(b) NORMAL AND SHEAR STRESS COMPONENTS (σ_{ix}, σ_{iy}, τ_{ixy}) AT A TYPICAL NODE i.

Fig. 5. Displacements and stresses at a typical node

In a one-, two- or three-dimensional state, the effective stress σ_{eff} is related to the stress components $\sigma_{ix}, \sigma_{iy}, \ldots$, by the expression

$$\sigma_{eff} = (I_{i1}^2 - 3I_{i2})^{1/2} \tag{1}$$

in which

I_{i1} = the first invariant of the stress tensor at node i

$= \sigma_{ix} + \sigma_{iy} + \sigma_{iz}$

I_{i2} = the second invariant of the stress tensor at node i

$= \sigma_{ix}\sigma_{iy} + \sigma_{iy}\sigma_{iz} + \sigma_{iz}\sigma_{ix} - \tau_{ixy}^2 - \tau_{iyz}^2 - \tau_{ixz}^2$

For the present example, σ_{ix}, σ_{iy}, τ_{ixy} are nonvanishing stress components. The σ_{eff} were computed by Eq. (1) for all the node points in the three materials of the model in Fig. 4. The results are plotted as the effective stress contours shown in Fig. 6.

The effective stress contour lines are the loci of points having the same level of effective stress. Each contour line in Fig. 6 is given a label 1, 2, 3, etc. The label indicates the effective stress level of a contour line. For example, the contour lines labeled 1 have an effective stress value of 344.7 N/cm² (500 psi), and the contour lines with label 2 have an effective stress value of 689.4 N/cm² (1000 psi) and so on. Whenever the spacing between contour lines allowed, an increment of 344.7 N/cm² (500 psi) was maintained from one line to the next; otherwise the increment was doubled.

This type of presentation provides a convenient pictorial means to easily examine the results. On the basis of the material properties in Table 1 and for the given geometry, temperature loading, and boundary conditions, the analysis predicts the following[2]:

(1) In the dark dotted area of the solder, $\sigma_{2eff} \geq \sigma_2^*$; i.e., complete failure will take place in this area under the conditions described.

(2) In the lightly dotted area only initial yielding will be reached ($\sigma_{2yield} \leq \sigma_{2eff} \leq \sigma_2^*$, where σ_{2yield} = yield stress in the solder). If the load increases, this area will have complete failure and additional yielding will set in adjacent areas.

(3) Areas where the effective stress contour lines are closely spaced have high effective stress gradient. Such areas are basically potential yield and subsequent failure areas. No failure was indicated in either the Kovar bus bar or the cell material.

Of course, the validity of the above results is dependent upon the accuracy of the assumptions, method of analysis, and the material property used. For example, within a temperature change of 80°C the material properties of Kovar, solder, and silicon change considerably. The properties in Table 1 provide, therefore, a rather crude representation of these properties. For this reason, the results obtained should be regarded as illustrative only.

D. Material Selection

It was previously noted that, among other factors, the material property variables E, ν, α of the various components of a cell array play an important role in component failures in the array. The remainder of this section illustrates this fact, and shows how the analysis can aid in material selection for cell arrays. Effects of geometry will be discussed in Section V-D.

[2]Subscripts 1, 2, 3 designate quantities associated with the bus bar, solder, and cell materials, respectively.

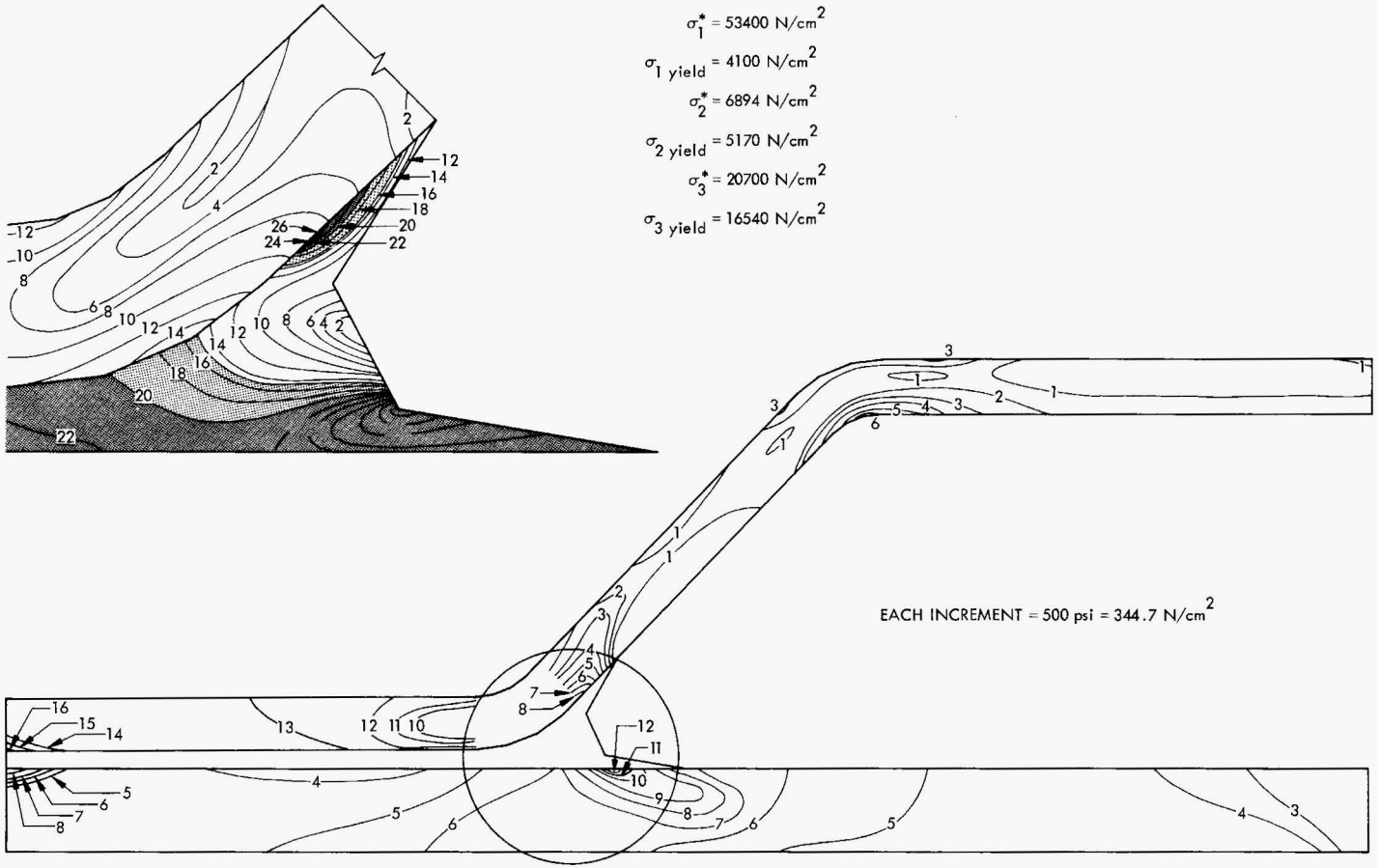

Fig. 6. Effective stress contours for example of thermal stresses in interconnectors

Table 2. Comparison of maximum effective stress for seven groups of candidate materials

Property	Group I	Group II	Group III	Group IV	Group V	Group VI	Group VII
E_1, N/cm^2	13.098×10^6	13.098×10^6	13.098×10^6	13.098×10^6	13.098×10^6	15.717×10^6	15.717×10^6
α_1, cm/cm/°C	5×10^{-6}	5×10^{-6}	5×10^{-6}	5×10^{-6}	5×10^{-6}	4×10^{-6}	4×10^{-6}
E_2, N/cm^2	4.136×10^6	4.136×10^6	4.136×10^6	4.136×10^6	4.136×10^6	3.309×10^6	3.309×10^6
α_2, cm/cm/°C	24×10^{-6}	24×10^{-6}	24×10^{-6}	24×10^{-6}	24×10^{-6}	19.2×10^{-6}	24×10^{-6}
E_3, N/cm^2	6.894×10^6	8.273×10^6	5.515×10^6	8.273×10^6	5.515×10^6	5.515×10^6	5.515×10^6
α_3, cm/cm/°C	2.9×10^{-6}	3.48×10^{-6}	3.48×10^{-6}	2.32×10^{-6}	2.32×10^{-6}	2.32×10^{-6}	2.32×10^{-6}
σ_{1eff}, N/cm^2	5848	5910	5767	5900	5767	4595	5021
σ_{2eff}, N/cm^2	11,960	11,944	12,124	11,944	11,975	6796	8621
σ_{3eff}, N/cm^2	4492	5053×10^3	4309	4560	4025	3077	3500

Table 2 lists seven different hypothetical groups of material properties for the bus bar, solder, and cell material. Subscripts 1, 2, 3 designate quantities associated with the bus bar, solder, and cell material, respectively. The first group of material properties is the original group of Table 1. All other groups have either the original values or $\pm 20\%$ change over the original values of the first group. Because Poisson's ratio ν varies only slightly from one candidate material to the other, its effect was excluded from the comparison by keeping it constant at $\nu = 0.3$. Contributions due to variations in the modeling procedure are also excluded by using the previously discussed model for the seven cases. Thus, the results shown in Table 2 for the maximum values of the effective stress σ_{eff} in each of the three materials 1, 2, 3, for each of the seven cases reflect contributions due to variations in (E_1, α_1), (E_2,α_2), and (E_3, α_3).

If the properties expressed in Table 2 represent true material properties for the seven groups of hypothetical candidate materials, group VI should be chosen. The predicted maximum effective stresses $\sigma_{1eff} = 4595$ N/cm^2, $\sigma_{2eff} = 6796$ N/cm^2, $\sigma_{3eff} = 3077$ N/cm^2 in each of the three materials of this group are less than the corresponding failure stresses $\sigma_1^* = 53400$ N/cm^2, $\sigma_2^* = 6894$ N/cm^2, $\sigma_3^* = 20680$ N/cm^2. Therefore, if group VI is used, chances of failure will be minimized.

Perhaps the chief contributing reason for the superiority of this group over other groups cited is the better match between the coefficients of thermal expansion α_1, α_2, α_3. This contribution is demonstrated by comparing σ_{2eff} in the solder in groups VI and VII. With all other properties kept the same, the coefficient of thermal expansion α_2 in group VI is 20% lower than its counterpart in group VII. This alone resulted in about 21.1% lower effective stress in the solder. Material property measurements are discussed in more detail in Section VI.

V. Pull Test Correlation With Analysis

A. Description of Pull Test

The pull test has been extensively used in the past as a means to mechanically qualify the strength of the cell/interconnect joints (Ref. 10). In this test, a metal bus bar tab as shown in Fig. 7 is bent in a configuration similar to that of Fig. 8 prior to soldering to the cell in Fig. 9. A tensile force is then applied to the standing portion of the tab. The force P^* that causes failure at the tab/cell interface is recorded as the contact strength. The test setup and typical test results are given in Figs. 10 and 11, which were taken from Ref. 10.

Contact strength values obtained from curves such as that of Fig. 11 are used for production purposes to accept or reject soldered connections in an array of solar cells.

B. Analysis of Pull Test

The pull test configuration was chosen here for the main purpose of checking the failure prediction analysis with results of the actual tests in Fig. 11. At room temperature, the average P^* is 17.65 N.

A finite element model of the test configurations of Figs. 8-10 is shown in Fig. 12. The same modeling procedure described previously is used in this case. Here again, the state of stress in the cell/tab connection is

predominantly plane stress state. In the model, the following have been assumed:

(1) The thin ohmic contact layer of titanium/silver on the cell is neglected for the reasons explained in Section III-A. The cell, therefore, is assumed to be made of one material whose mechanical properties are those of single-crystal silicon.

(2) The clamping fixture in Fig. 10 is replaced in the model by suppressing the displacement degrees of freedom at the bottom surface. This type of boundary displacement produces the same effect as the clamping fixture.

The total number of elements used in the model is 243: 63 elements in the Kovar bus bar, 88 elements in the solder, and 92 elements in the cell. The 243 elements are connected together at 274 node points. By allowing two displacement degrees of freedom at every node and suppressing these degrees of freedom at the bottom surface of the cell, the total number of unknowns is reduced to 500 displacement degrees of freedom.

With the model of Fig. 12 and the material properties of Table 1 for room temperature, the invariant effective stresses at the 274 nodes were computed according to Eq. (1) for $P^* = 17.65$ N.

C. Results

The effective stress contours for the pull test configurations are shown in Fig. 13, in which the labels 1, 2, 3, etc., again indicate the effective stress level. For this case, however, each labeling increment corresponds to 689.4 N/cm² (1000 psi). For example, labels 9 indicate 6204.6 N/cm² (9000 psi) for the effective stress, and labels 10 indicate a 6894.0 N/cm² (10,000 psi) for the effective stress, etc.

On the basis of Fig. 13, the following conclusions can be made:

(1) Under the applied load of 17.65 N, no failure is predicted in either the Kovar bus bar or the cell. The computed maximum effective stress in the bar is only 26886. N/cm² (39,000 psi), in comparison with the failure effective stress $\sigma_1^* = 53{,}400$ N/cm² (77,500) psi). Also, the computed maximum effective stress in the cell is 5756.0 N/cm² (8350 psi) compared with σ_2^* of at least 20,680 N/cm² (30,000 psi) according to Section V.

(2) Failure in the dark dotted area and initial yielding in the lightly dotted area is predicted when the 17.65-N load is applied. In the predicted failure area, the failure stress $\sigma_2^* = 6894.0$ N/cm² (10,000 psi) was exceeded. The computed maximum effective stress in the solder is 8960 N/cm² (12,940 psi).

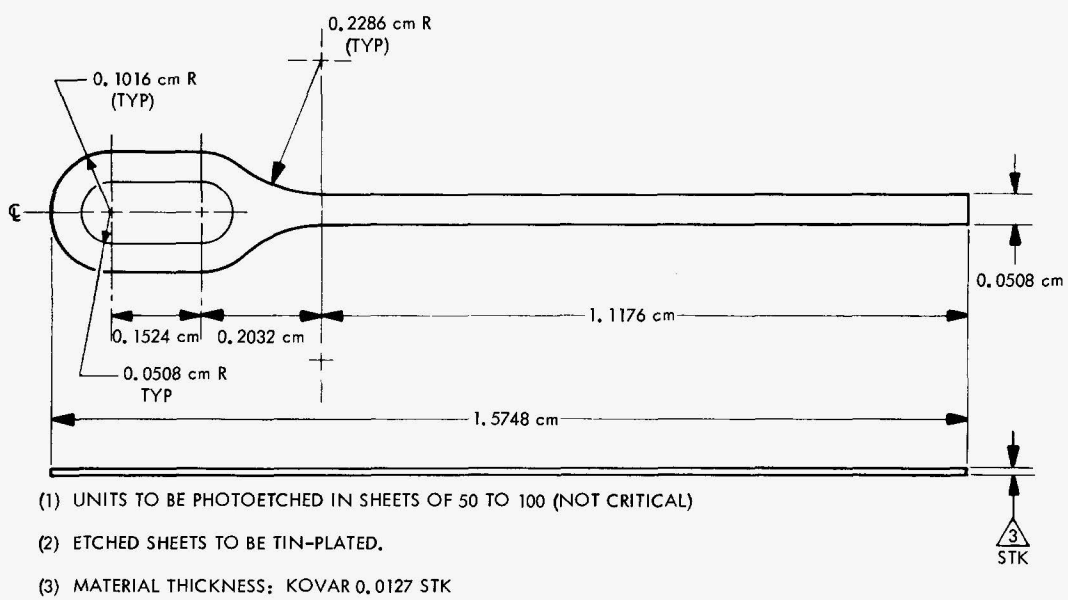

Fig. 7. Solar cell ohmic contact strength test tab

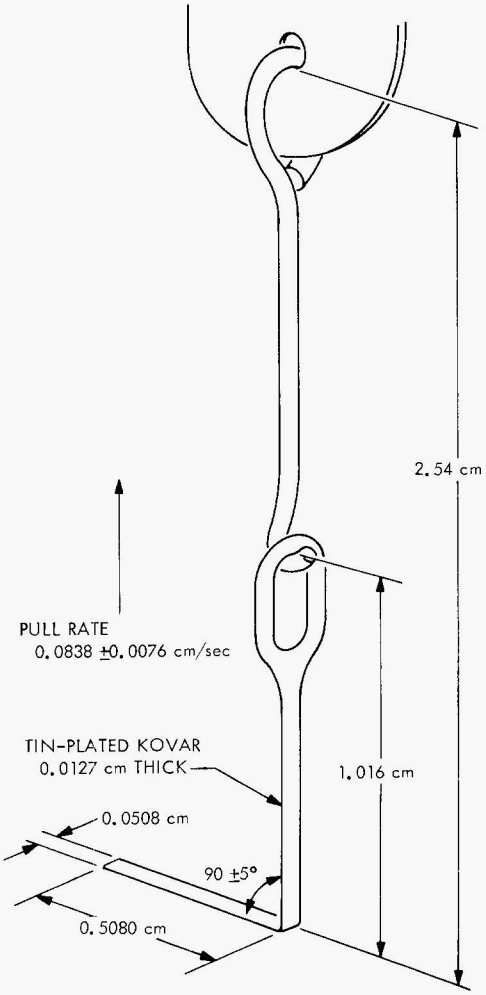

Fig. 8. Contact strength test configuration

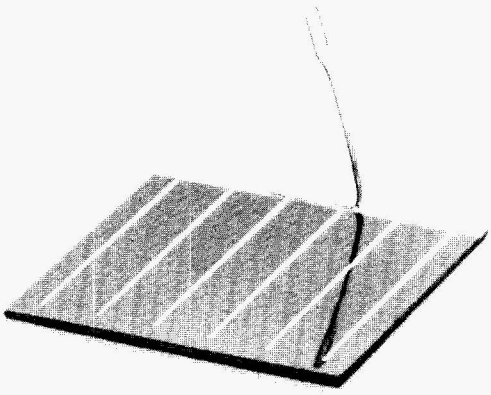

Fig. 9. Typical solar cell with contact strength tab soldered

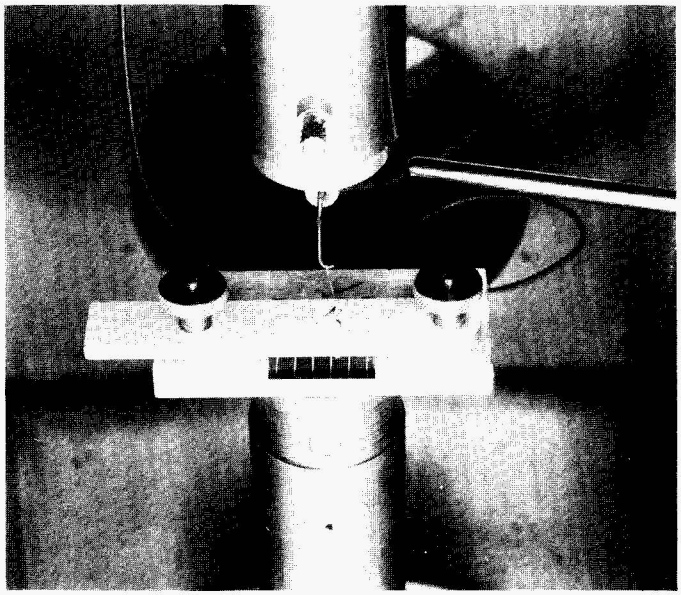

Fig. 10. Solar cell mounted in materials testing machine prior to contact strength test (Note that the thermocouple is positioned between the cell and mounting fixture)

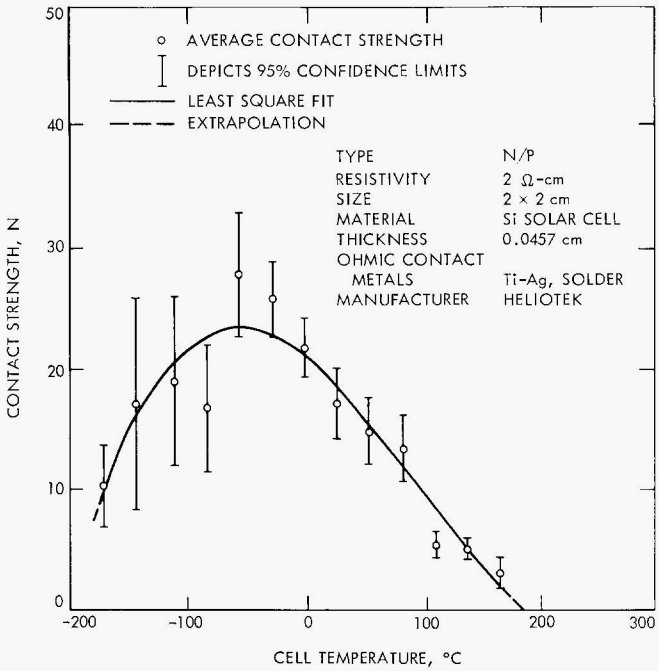

Fig. 11. N-contact strength of solar cells as a function of temperature

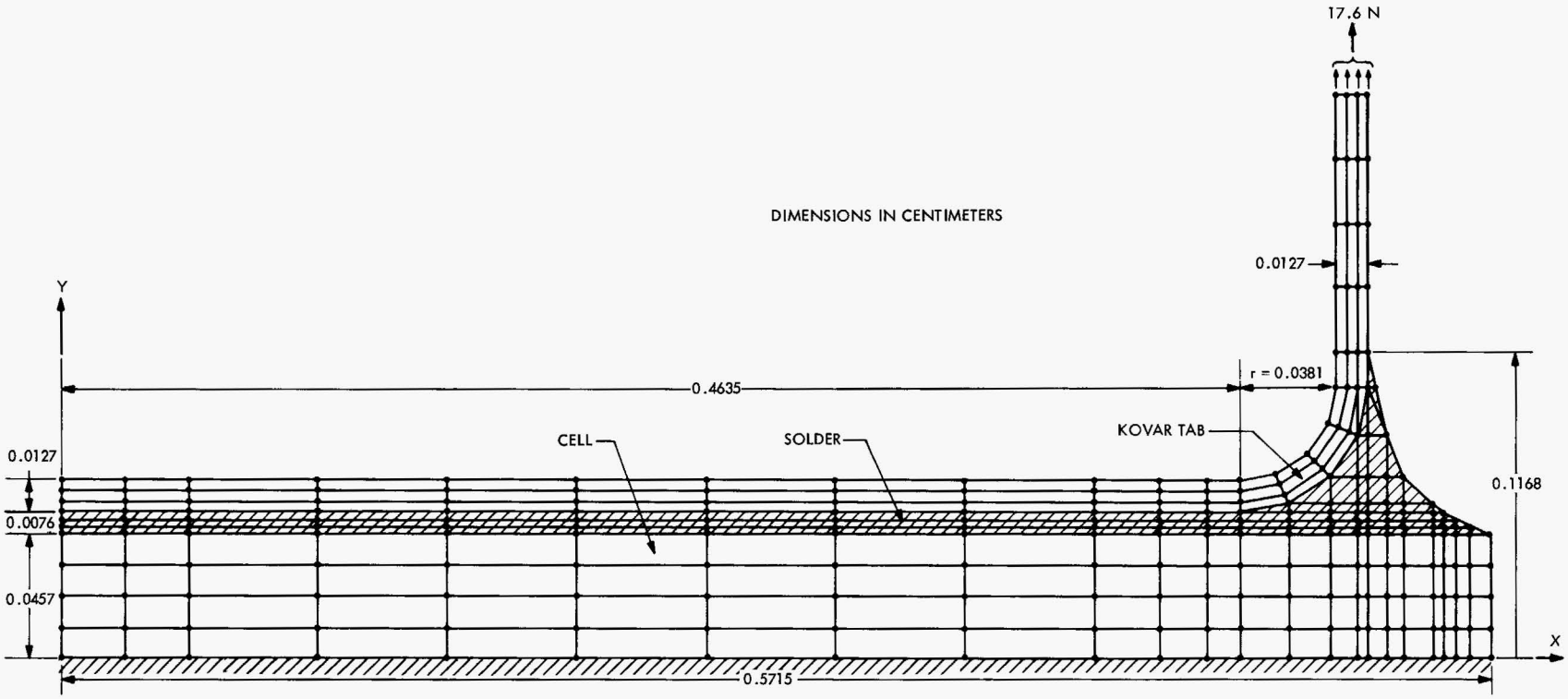

Fig. 12. Finite element model of contact strength test configuration

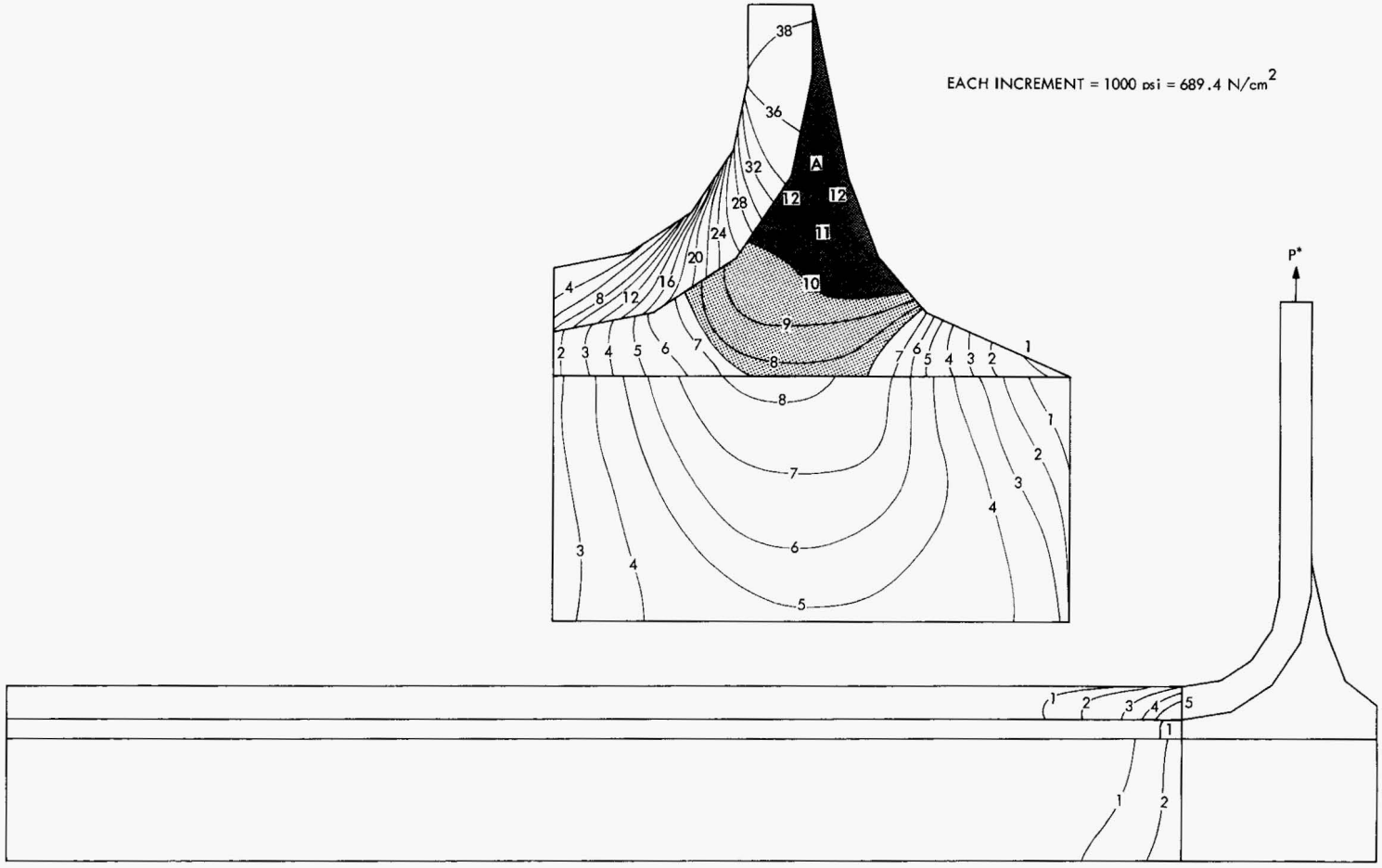

Fig. 13. Stress contours in pull test configuration

D. Effect of Geometry on Contact Strength

Section IV-D illustrated how the analysis can be used to select the proper materials for a given bus bar/cell geometry. A similar procedure can be also used to introduce the proper geometry changes to reduce the effective stresses. The changes can be in thickness or in overall geometry of the components of a bus bar/cell arrangement. In deciding upon the necessary changes, the designer needs to consult the effective stress contours, such as those of Figs. 6 and 13 as well as the computed stress components σ_{ix}, σ_{iy}, τ_{ixy}, . . . , from which the stress contours are constructed. These quantities together provide a reasonable guide for implementing the necessary changes.

To illustrate, consider the pull test configuration. As Fig. 13 shows, all shaded areas have high effective stresses. According to Eq. (1), the effective stress invariant is a function of the stress components (in this case, the planar normal and shear stress σ_{ix}, σ_{iy}, τ_{ixy}). For example, at point A in the predicted failure area of Fig. 13, an effective stress of 7928 N/cm² (11,500 psi) resulted from σ_{Ax} = 837.6 N/cm² (1215 psi), σ_{Ay} = 6976.7 N/cm² (10,120 psi), and τ_{Axy} = 2528 N/cm² (3667 psi). Other points in the area had different values for σ_{ix}, σ_{iy}, τ_{ixy}, but σ_{iy} always had the largest value of the three components. A geometry change that can bring about significant reduction in the effective stresses in the failure region would then involve increasing the solder cross-sectional area normal to the Y-axis (i.e., by adding more solder to the fillet in the X-direction).

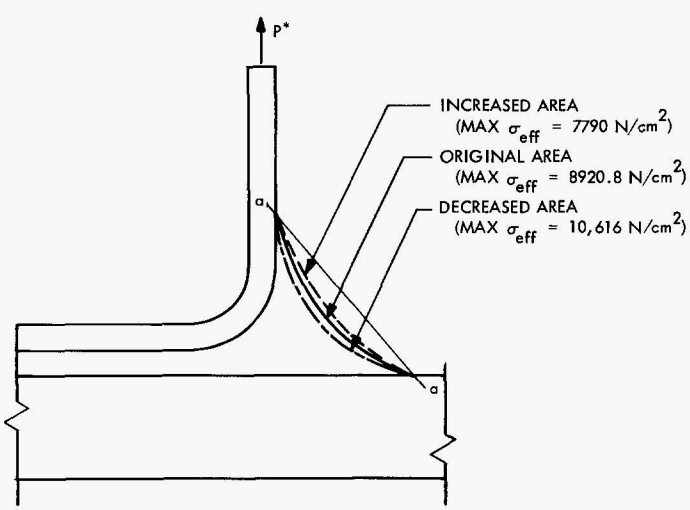

Fig. 14. Effect of geometry changes on contact strength

Figure 14 shows three geometries of the solder fillet area. The solid curve represents the original fillet geometry of Figs. 12 and 13, while the other two broken curves represent an increase and a decrease in the fillet area (obtained by adding to the original curve ±20% of the distance between the cord line aa and the original curve). The curve depicting increased solder resulted in a maximum effective stress in the solder of 7790 N/cm² (11,300 psi), while the curve depicting decreased solder exhibited a maximum effective stress in the solder of 10,616.7 N/cm² (15,400 psi). These are compared with the maximum effective stress value 8920.8 N/cm² (12,940 psi) in the original geometry of Fig. 13. Further addition of solder in the X-direction can further reduce σ_{eff} below the failure stress σ^*.

This numerical example calls for three additional remarks:

(1) By similar reasoning, one can make the proper geometry changes for any given design and loading conditions, thermal or mechanical.

(2) The pull test results (Ref. 10) indicate that, at room temperature, variability in the failure modes was observed. In some cases failure in the solder region took place; while in others, pieces of silicon adhering to the titanium/silver–solder were pulled from the cell. Reference 10 also attributed the variability in the results to inconsistencies in the manufacturing process, e.g., variation in the solder area. The failure mode predicted by the analysis is one in which separation in the dark area of the solder (Fig. 13) will take place first. As the load increases, a failure mechanism will develop as a result of this region propagating toward the cell, at which time the effective stresses in the cell would have increased up to its failure limit. The sensitivity of the pull test values P^* to the solder fillet geometry was suggested by the test data and was also confirmed by the present example. Results of the present example tend to agree reasonably well with the test data. It seems premature, however, to conclude that failure could have been initiated by the titanium/silver layer had it been included in the analysis.

(3) A more meaningful pull strength P^* value to use as a production control parameter can be obtained from analysis. Provided that the soldering technique is satisfactory, these pull strength values should be achieved when the solder fillet geometry and material properties of the cell and interconnects are specified.

VI. Material Properties

The material properties of concern in performing structural design studies of solar cell interconnects include both thermal and mechanical. As previously mentioned, the specific properties of interest are the modulus of elasticity, Poisson's ratio, ultimate strength, and coefficient of expansion. Since most of the materials of the solar cell/interconnect construction are considered to be nonstructural, very little data is available on their mechanical properties, especially at cryogenic temperatures. Some thermal property data was recorded, but in most cases the temperature range over which these properties were measured was not broad enough in scope. The above properties are needed over the temperature range −200 to +200°C.

As a result, tests were required on most of the materials used in solar arrays to obtain the necessary mechanical and thermal properties. Emphasis was first placed on obtaining data on the single-crystal silicon solar cell material. Initially, the room temperature, three-point bend (flexural) tests were performed on bare (no contacts or coatings) silicon solar cell wafers to obtain mechanical properties.

Subsequently, linear thermal expansion tests were made on single-crystal silicon and on silicone rubber adhesives used for the solar cell to cover glass and solar cell to substrate bonds. These tests are described in the following paragraphs. The silicon wafers for these tests were obtained from both Centralab and Heliotek. The silicone rubber adhesives were from the General Electric Co. and Dow Corning Corp.

A. Flexural Testing of Silicon Solar Cell Wafers

Room temperature three-point bend tests were performed on solar cell wafers, representative of various processing methods. The wafers were 1 × 2-cm rectangles or 2 × 2-cm squares with nominal thicknesses of 0.4 mm. Tests were made on the Heliotek wafers that had been removed from the manufacturing cycle at various points in solar cell processing, e.g., bare blanks as well as some with SiO coatings and vacuum-deposited titanium/silver contacts (but without bus bars). No complete Centralab cells were included for test. Instead, a variety of differently processed, bare wafers were tested. Tests were conducted using the procedures of Federal Test Standard No. 406, Method 1031. Appendix A gives the procedure for the tests and the theoretical considerations for calculating the failure stress σ^* and the elastic modulus E in flexure from the three-point bend test data.

Initially tests were conducted on P-type wafers with a phosphorous-diffused layer (N/P). On this group it was noted that the wafers were bowed (convex) on the polished, diffused side, apparently as a result of the phosphorous diffusion or wafer slicing procedures. This anomaly was not observed on the remainder of the wafers tested from either manufacturer. The extent of bowing was measured on seven cells and was determined to vary from a minimum of 0.013 mm (0.0005 in.) to a maximum of 0.051 mm (0.002 in.). This prestressed condition on the wafer accounted for the wafers being almost twice as strong (breaking stress) when loaded in the direction opposite the bow (46,500 N/cm^2, 67,500 psi) as when loaded in the direction of the bow (20,700 N/cm^2, 30,000 psi). Scatter was noted in the breaking stress values for all wafers; e.g., in the first group of bowed wafers, the low value was 10,525 N/cm^2 (15,300 psi) and the high value was 28,100 N/cm^2 (40,800 psi). In a second group of bowed specimens, the high was 59,700 N/cm^2 (86,800 psi) and the low was 28,800 N/cm^2 (41,800 psi).

Some scatter was also present in the elastic modulus determinations but not to the same extent. For the breaking stress determinations the scatter is attributed to edge effects and stress raisers in the wafers in the form of microcracks, sharp edges and nicks. Table 3 gives results on various types of silicon wafers from Heliotek. A total of 76 Heliotek wafers were tested.

Similar three-point bend tests were performed on Centralab solar cell wafers. Some of these wafers were N-type, 1 × 2 cm in dimension, while the majority were P-type, 2 × 2 cm. Again all wafers had a nominal thickness of 0.4 mm. Results are shown in Table 4. In all tests conducted, a minimum of three wafers representative of a particular process procedure or silicon type was tested with the polished side in compression and another three with the polished side in tension.

B. Thermal Expansion Tests on Silicon and Silicone Rubber Adhesives

General Dynamics (Convair Division) under contract to JPL, performed linear thermal expansion measurements on the solar cell silicon material and various silicone rubber adhesives. The thermal expansion testing was conducted at temperatures from −196 through +200°C. Single-crystal silicon solar cell material 0.3 × 1.3 × 5.1 cm (0.118 × 0.5 × 2.0 in.) was provided

Table 3. Results of three-point bend tests on Heliotek solar cell wafers

Specimen type	Number tested	Average failure stress σ^*, N/cm^2 × 10^3 (psi × 10^3)		Average elastic modulus E^a, N/cm^2 × 10^6 (psi × 10^6)	
		Polished side (grid) in tension	Polished side (grid) in compression	Polished side (grid) in tension	Polished side (grid) in compression
N/P 10 Ω-cm complete cells, Ag contacts and SiO coating[b]	6	21.6 (31.3)	25.8 (37.4)	4.6 (6.6)	4.5 (6.5)
10 Ω-cm P-type bare wafers[b]	6	37.2 (54.0)		6.5 (9.4)	
P/N, CG 8-8-10 boron-diffused, lapped blanks, complete cells	5	17.8 (25.8)	19.1 (27.7)	7.2 (10.4)	6.4 (9.3)
P/N Lopex 8-8-10, boron-diffused, lapped blanks, complete cells	6	22.3 (32.3)	25.5 (37.0)	7.1 (10.3)	7.7 (11.1)
P/N, CG complete cells (etched Si)	6	22.2 (32.2)	15.9 (23.0)	7.4 (10.7)	6.6 (9.5)
P/N Lopex complete cells (etched Si)	6	14.2 (27.6)	22.6 (32.8)	9.7 (14.1)	8.6 (12.5)
P/N Lopex complete cells, lithium-diffused (etched Si)	6	21.9 (31.7)	6.3 (9.1)	8.1 (11.8)	5.8 (8.4)
P/N CG complete cells, lithium-diffused (etched Si)	6	20.8 (30.2)	9.4 (13.6)	6.6 (9.5)	7.1 (10.3)
N-type CG blanks (etched Si)	5	32.3 (46.8)		8.3 (12.1)	
N-type float zone blanks (etched Si)	5	26.3 (38.1)		9.0 (13.0)	
N-type Lopex blanks (etched Si)	5	21.5 (31.2)		7.4 (10.7)	
N/P wafers (first submittal of 2 × 2 cm wafers)[b]	14	20.7 (30.0)	46.5 (67.5)	5.9 (8.5)	8.4 (12.2)

[a]E calculated from deflection and load at approximate midpoint in load-deflection curve or where curve appeared most linear.

[b]2 × 2-cm cells; all others were 1 × 2-cm cells.

Table 4. Results of three-point bend tests on Centralab solar cell wafers

Specimen type	Number tested	Average breaking stress σ^*, N/cm^2 × 10^3 (psi × 10^3)		Average elastic modulus E^a, N/cm^2 × 10^6 (psi × 10^6)	
		Polished side in tension	Polished side in compression	Polished side in tension	Polished side in compression
N-type, undiffused	6	15.7 (22.7)	11.2 (16.3)	8.1 (11.8)	6.1 (8.9)
N-type, lithium diffusion on etched side	10	18.6 (27.0)	7.8 (11.3)	8.2 (11.9)	6.0 (8.7)
P-type, 3 Ω-cm undiffused	6	11.7 (17.0)	11.1 (16.1)	4.0 (5.8)	3.8 (5.5)
P-type, 3 Ω-cm P diffusion	10	16.5 (24.0)	9.6 (14.0)	4.8 (6.9)	3.7 (5.4)
P-type, 10 Ω-cm undiffused	6	13.3 (19.3)	7.2 (10.4)	4.8 (6.9)	4.3 (6.3)
P-type, 10 Ω-cm P diffusion	10	12.5 (18.1)	13.2 (19.1)	5.5 (8.0)	4.3 (6.3)

[a]E calculated from deflection and load at approximate midpoint in load-deflection curve or where curve appeared most linear.

Notes:

1. Values listed are average of a minimum of three and a maximum of five wafers tested.
2. P-type wafers were cut parallel to the [100] crystal growth axis, but orientation is not maintained; all wafers not from same ingot.
3. N-type wafers cut parallel to the [111] crystal growth axis and orientation maintained.

by Centralab for these measurements. The types and processing variables represented on the silicon specimens along with the silicone rubber adhesive specimens are shown in Table 5. The silicon samples were cut to size with diamond saws, cleaned and lightly etched with a nitric-hydrofluoric acid solution. The N-type silicon was oriented with the longitudinal axes of the specimens parallel to the [111] growth axis of the material while the P-type were cut with their longitudinal dimension parallel to the [100] growth axis.

The adhesive specimens were vacuum-cast at JPL in 5.1-cm (2-in.) lengths and diameters of 0.81 cm (0.320 in.). General Dynamics cut these specimens of RTV 41, RTV 560, RTV 566, RTV 602, DC 93-500 and XR 63-489 into shorter lengths for their tests. All adhesive specimens were preconditioned by a stabilizing treatment of three thermal cycles from +200 to −196°C prior to their submittal to General Dynamics. The purpose of the preconditioning was to assure that all material reactions that would occur over this temperature span had in fact gone to completion and that only thermal effects were being measured during the test. The coefficient of expansion measurements were performed on a modified Leitz quartz dilatometer. The test procedures used by Convair for the thermal expansion measurements are described in Appendix B.

The results from the linear thermal expansion tests were presented in tabular form and in plots of $\Delta L/L$ vs temperature. The plots for the silicon specimens are very similar and indicate that the thermal expansion of solar cell grade silicon is affected very little by the addition of doping elements such as boron and phosphorous during diffusion treatments to grow P-N junctions. In addition, the resistivity magnitude and the crystal growth orientation also had no significant effects on the thermal expansion.

The data was compiled and an average determined from the 16 silicon samples (Fig. 15). Figure 15 also shows data points for the Corning 7940 fused silica cover glass material. The data for the fused silica was provided by Corning Glass Works.

The results for the silicone rubber adhesives are shown in Fig. 16. As seen in this figure, there is a definite decrease in the slopes of the expansion curves at around −125°C. For most silicone elastometers, −125°C is the glass transition temperature. Two of the silicone rubber

Table 5. Specimens tested for linear thermal expansion

Material description	Number tested	Identification
N-type silicon, 30 Ω-cm, undiffused (control)	2	N30G
N-type silicon, 30 Ω-cm, normal lithium diffusion (one side)	2	N30C
N-type silicon, 30 Ω-cm, hyper lithium diffusion (both sides)	2	N30E
N-type silicon, 30 Ω-cm, B diffused (P/N)	2	N30A
P-type silicon, 3 Ω-cm, undiffused (control)	2	P3C
P-type silicon, 3 Ω-cm, P diffused (N/P)	2	P3A
P-type silicon, 10 Ω-cm undiffused (control)	2	P10C
P-type silicon, 10 Ω-cm P diffused (N/P)	2	P10A
RTV 41/T-12 (polydimethylsiloxane)	2	–
RTV 560/9808 (polyphenylmethylsiloxane)	2	–
RTV 566 A/B (polyphenylmethylsiloxane)	2	–
RTV 602/SRC-05 (polydimethylsiloxane)	2	–
DC 93-500 (polydimethylsiloxane)	2	–
XR 63-489 (polydimethylsiloxane)	2	–

materials, RTV 602 and RTV 41, show indication of beginning glassy transition at about −50°C. The glass transition temperature may be defined as that temperature at which the molecular alignment of the silicone assumes that of glass or other crystalline materials. These temperatures (−50 and −125°C) coincide with reported glass transition temperatures for these silicone rubber adhesives.

C. Discussion of Test Results

The results of the flexural tests on the Centralab and Heliotek single-crystal silicon wafers were appreciably different. Tables 3 and 4 show the Heliotek samples had higher breaking strengths. The overall average breaking strength of the Heliotek wafers tested with the outer fibers of the polished surface in tension was 20,700 N/cm^2 (30,200 psi). With this surface in compression, the overall average strength was 17,800 N/cm^2 (25,800 psi). These values were 14,700 N/cm^2 (21,300 psi) and 10,000 N/cm^2 (14,500 psi), respectively, for the Centralab wafers. The average values include wafers with the various diffusions and both N- and P-type material. Also included are wafers with lithium (Li) diffusion on the back surface. It is of special note that the Li diffusion decreased the breaking strengths of wafers from both vendors with diffused surface in tension. More scatter was noted in the individual data points for the Centralab tests than for the Heliotek. This is directly attributable to the original surface conditions of the wafers. The rougher (chemically etched and sandblasted) bottom surfaces of the Centralab wafers were found to contain many microfissures and cracks when examined at high magnifications with a scanning electron microscope. These cracks behaved as stress risers when this surface was stressed in tension, resulting in lower breaking strength values for the brittle silicon wafers. In addition, the sides of Centralab wafers were also sandblasted with resultant rough edges and microcracks which further reduced their strength and contributed to the scatter in the data. In comparison, the Heliotek wafers received more chemical polishing in their preparation than the Centralab wafers. Chemical polishing produces a surface with lower residual stress, as shown by the results of these tests. The sketch below is an exaggerated presentation of the profiles of wafers from the two vendors. Figure 17 shows photomicrographs of the edges of the two vendors' wafers taken with a scanning electron microscope (SEM).

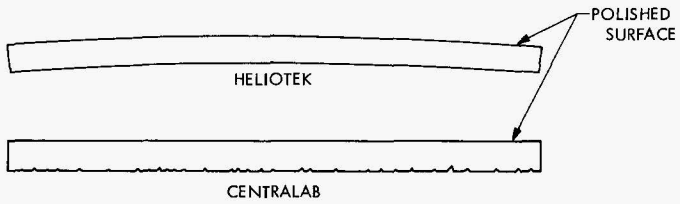

The values for the elastic modulus E were calculated from the three-point bend test data determined from load-deflection curves, Tables 3 and 4. For purposes of mathematical modeling, the elastic modulus from dynamic stress-strain measurements is required, and further testing of bulk solar cell grade silicon is underway to determine this as well as other mechanical properties, e.g., ultimate tensile and compressive strength σ^* and Poisson's ratio ν.

The thermal expansion test results are shown as Figs. 15 and 16. As pointed out earlier, these tests indicate that the bulk silicon properties predominate in determining its thermal behavior. Since electrical resistivity and conduction type (P or N) is determined by very minute (ppm) additions of impurity elements, it is not surprising that they would not have a significant effect on the linear thermal expansion. However, it should be remembered that the objective of these tests was to obtain quantitative data on solar cell grade silicon and other interconnect materials.

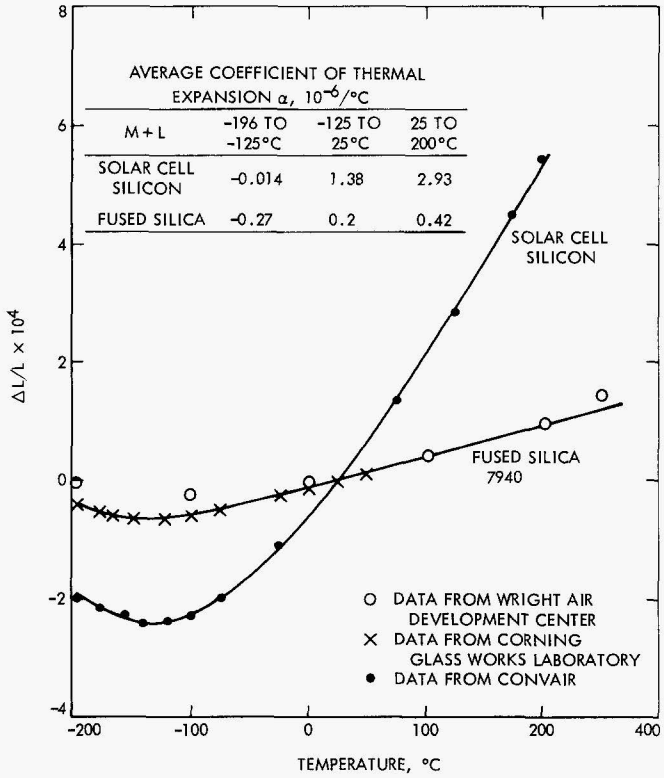

Fig. 15. Thermal expansion of solar cell silicon and fused silica cover glass

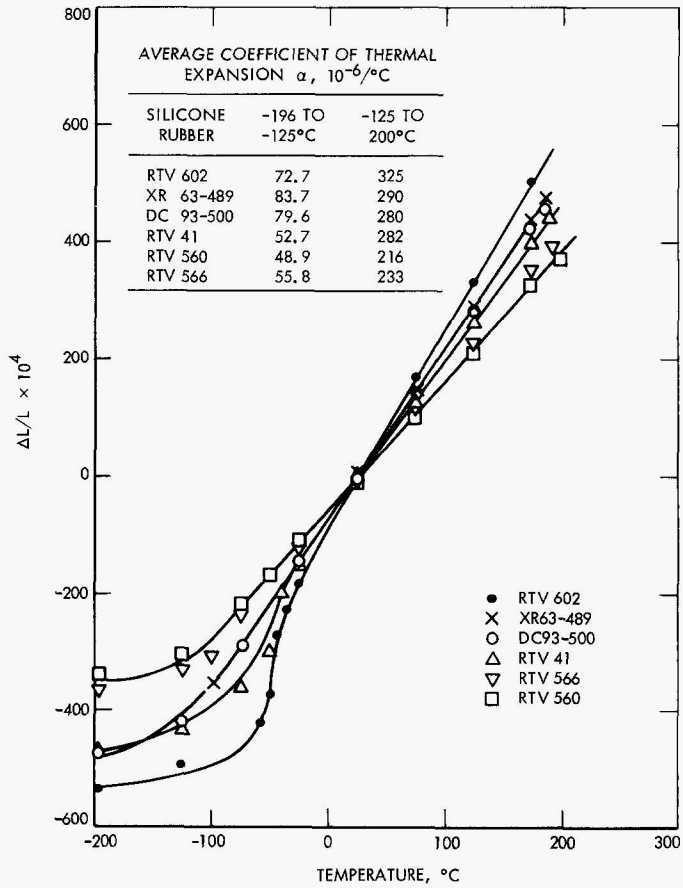

Fig. 16. Thermal expansion of solar cell/cover glass and solar cell/substrate silicone rubber adhesives

The values for the average coefficient of linear expansion α for silicon agree with those found in the literature (Refs. 11–13) at some of the temperatures. Another investigator (Ref. 14) has also reported that the crystal growth orientation of the silicon had no significant effect on this property. The data shown in Fig. 15 defines the shape of the thermal expansion curve for the silicon. Between −125 and −196°C the slope of the fused silica curve closely approximates that of the silicon. In the portion of the curve between −100 and −200°C, measurements were made in 20°C increments to determine accurately where the negative coefficient occurred.

The data on the silicone rubber adhesives basically illustrates that two of the dimethyl compounds (RTV 41 and RTV 602) undergo an earlier transition to the glassy brittle phase at subzero temperatures. These two materials have been used extensively in the past with good success, but at lower temperature extremes. The other dimethyl compounds (which comprised all but the RTV 560 and RTV 566 in these tests) have greater expansion extremes (Fig. 16) at each end of the temperature scale. The methyl-phenyl compounds (RTV 560 and RTV 566) have the least expansion. The latter materials are not as brittle at these low temperatures and are also known to show less change in their room temperature properties at elevated temperatures than the dimethyl compounds.

The test procedures used in conducting the thermal expansion tests were to place the specimen in the test chamber, cool to −196°C within 15 min and stabilize at that temperature for 2 h. Measurements were made on the heatup cycle, usually in 50°C increments, to +200°C. The time at each temperature increment was from 10 to 20 min, representing a rather slow heating rate in comparison to what might happen during a sun occultation on a space flight. The effects of the cooling and heating rates on material contraction and expansion characteristics were not investigated during this portion of the program. Work by other investigators, however, has shown that the rate of change of temperature, up to 35°C per min, was relatively unimportant in causing failed interconnections during a thermal cycling test program on solar cell panels (Ref. 15).

CENTRALAB N-TYPE
UNDIFFUSED,
30 ohm-cm

HELIOTEK P-TYPE,
P DIFFUSED,
2 ohm-cm

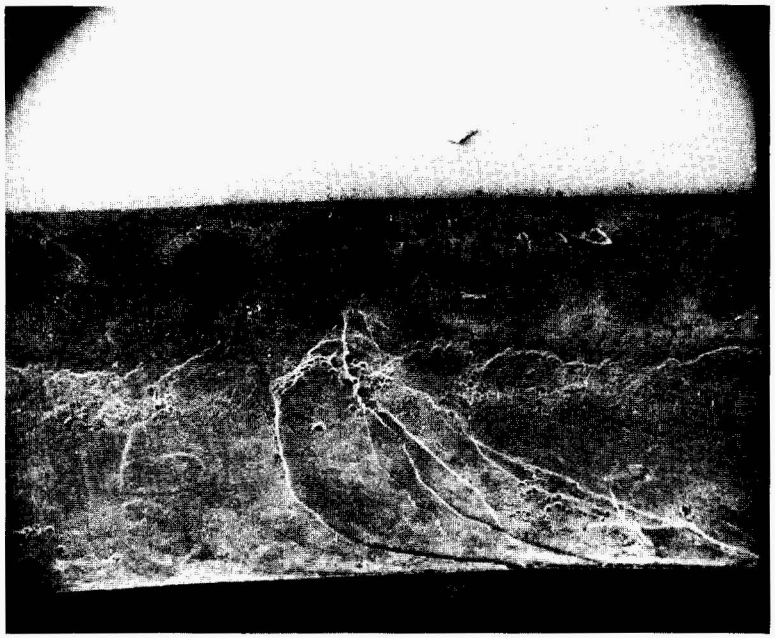

Fig. 17. Scanning electron microscope photographs of edges of Centralab and Heliotek silicon solar cell wafers (×240)

Table 6. Outgassing properties of candidate adhesives for solar cell/substrate and solar cell/cover glass bonds

Manufacturer	Material	Outgassing	
		Total weight loss, %	Volatile condensible materials, %
General Electric	RTV 41/T-12	2.0	0.5
General Electric	RTV 560/9808	3.0	0.5
General Electric	RTV 566 A/B	0.20	0.02
General Electric	RTV 602/SRC-05	3.10	0.96
Dow Corning	DC 93-500	0.22	0.02
Dow Corning	XR 63-489	1.4	0.6

Mechanical and thermal properties of silicone rubber adhesives are very important considerations. However, these materials must possess other important properties. They must be adaptable to production line solar array assembly techniques; e.g., they must have a reasonable pot life and working viscosity. In addition, they must be low in the production of outgassing products in a vacuum environment. Data is shown in Table 6 on the various candidates with respect to behavior in vacuum. The more a material outgasses, producing larger amounts of volatile condensable materials, the more the chance that the solar cell efficiency might drop because of these materials condensing on the cooler cover glass surfaces or other critical areas of the spacecraft. The subject of outgassing of polymeric materials is discussed in more detail in Appendix C.

VII. Conclusions and Direction of Future Work

A. Conclusions

The main advantage of the finite element technique used in this report is its versatility in handling various designs with different geometries and material properties. The procedure makes it possible to analyze almost any design configuration with as many as 99 different material properties. Introducing changes in configuration or material properties for the purpose of optimizing the design is a simple matter.

The components of stresses obtained from the finite element analysis, along with the effective stress contours based on the von Mises failure criterion (or any other suitable criterion) and the mechanical and thermal material properties, provide the solar cell array designer with the necessary information which enables him to rationally approach the optimization of a particular design. The optimization of the design involves selecting the best combination of compatible materials for the array's components (as illustrated in Section IV) and introducing the proper geometry changes (as illustrated in Section V). From a structural integrity point of view the optimum design is that which can successfully survive the array's environment during its lifetime. Of course, it is desirable to use the least amount of material in the design and to produce a design which is easy to manufacture.

The design procedure and rationale discussed throughout this report was aimed at eliminating much of the guessing on the designer's part and replacing it with a more sound methodology, thus converting the design of solar cell arrays to a more reliable and less costly process.

As pointed out, the success of this approach relies heavily on the availability of basic material properties of components of the cell array. Some of these properties were determined in this phase of the program. Significant data was obtained concerning the thermal behavior of the silicon solar cell material and the dimethyl and phenylmethyl silicone materials. The thermal test results show wide deviations (by a factor of 10 or more) between the expansion of the solar cell silicon and the adhesives at the various temperatures. The rate of change in linear dimensions is significantly higher for the silicone materials. Ultimately the other stress governing factors will be determined. These factors are: the optimum adhesive thicknesses and the changes in modulus of elasticity with temperature for the silicon, the adhesives, the cover glasses and the substrates. The properties obtained to date are a portion of this data file, and it is too early yet to make any definite conclusions.

The results do indicate, however, that the orientation of the crystalline structure of the silicon cell with respect to its geometry, e.g., whether or not the wafer is sliced parallel to a particular crystal growth axis, has no significant effect on its thermal expansion. In addition, the concentration levels of impurity atoms added to the silicon crystal lattice that determine its electrical behavior characteristics (making it either P- or N- conductivity type) have no apparent effect on its thermal expansion. The flexural tests (three-point bend) show that the silicon wafer is very sensitive to processing variables. Small stress concentrators such as surface microcracks and fissures resulting from mechanical polishing and sandblasting during cell fabrication dramatically lower flexural strength. These findings emphasize that better process

control on the part of the solar cell manufacturer is needed to assure optimum strength cells.

B. Recommendations for Future Work

There are several areas in the analysis and material properties determination that require additional work. The most important of these are:

(1) Expansion of the current analysis procedure to account for thermal cycling.

(2) Three-dimensional modeling of solar cell/interconnect and its analysis along with the two-dimensional model in a thermal cycling scheme.

(3) Additional material properties and data compilation at cryogenic and elevated temperatures.

(4) Comparison between analytical prediction and actual testing.

References

1. *Development of An Integrated Lightweight Flexible Silicon Solar Cell Array*, Final Report, prepared under JPL Contract No. 952560, Heliotek (a division of Textron, Inc.), Sylmar, Calif., 1970.
2. Final Report, Document No. 4039, prepared under JPL Contract No. 952485, Electro Optical Systems (a division of Xerox Corp.), Pasadena, Calif., 1970.
3. *Study to Establish Criteria for a Solar Cell Array for Use as a Primary Power Source for Lunar-Based Water Electrolysis System*, Final Technical Report prepared under G. C. Marshall Space Flight Center Contract No. NAS 8-21189, TRW Systems Group, Los Angeles, Calif., Dec., 1970.
4. *Surveyor Sample Panel Test Report*, Report 7050-TR-4, prepared under JPL Contract No. 951488, Electro Optical Systems (a division of Xerox Corp.), Pasadena, Calif., March 1967.
5. Butterworth, L. W., and Yasui, R. K., *Structural Analysis of Silicon Solar Arrays*, Technical Report 32-1528, Jet Propulsion Laboratory, Pasadena, California, May 1971.
6. Zienkiewicz, O. C., and Cheung, Y. K., *The Finite Element Method in Structural and Continuum Mechanics*, McGraw-Hill Publishing Company, New York, 1967.
7. Utku, S., and Akyuz, F., *Elas—A General Purpose Computer Program for the Equilibrium Problems of Linear Structures: User's Manual*, Technical Report 32-1240, Vol. I, Jet Propulsion Laboratory, Pasadena, Calif., Feb., 1968.

References (contd)

8. Melosh, R., Diether, P., and Brennan, M., *Structural Analysis and Matrix Interpretive System (SAMIS) Program Report*, Technical Memorandum 33-307 (prepared for JPL by Philco Corp.), Jet Propulsion Laboratory, Pasadena, Calif., Sept. 1, 1966.

9. McCormick, C., Editor, *The NASTRAN User's Manual*, NASA SP-22, Washington, D.C., Sept., 1970.

10. Schmidt, L. W., and Yasui, R. K., "Performance Characteristics of Titanium-silver Contact N/P and P/N Silicon Solar Cells," Records of the 8th Photovoltaic Specialist Conference, IEEE, held at Seattle, Washington, August 1970, pp. 110-122.

11. Touloukian, Y. S., Editor, *Thermophysical Properties of High Temperature Solid Materials, Vol. 1: Elements*, Purdue Research Foundation, Purdue University, Indiana, 1967.

12. Straumanis, M. E., et al., "Perfection of the Lattice of Dislocation-Free Silicon, Studied by the Lattice-Constant and Density Method," *J. Appl. Phys.*, Vol. 32, No. 7, July 1961, pp. 1382–1384.

13. Maissel, L., "Thermal Expansion of Silicon," *J. Appl. Phys.*, Vol. 31, Jan–June 1960, p. 211.

14. Gibbons, D. F., "Thermal Expansion of Some Crystals with the Diamond Structure," *Phys. Rev.*, Vol. 112, No. 1, Oct., 1958.

15. Luft, W., and Maiden, E. E., "Temperature Cycling Effects on Solar Panels," IEEE Transactions on Aerospace and Electronic Systems, Vol. AES-5, No. 6, Nov., 1969.

Appendix A

Procedures for Three-Point Flexure Tests and Calculation of Mechanical Properties

Testing was performed at room ambient temperatures using an Instron testing machine in conjunction with a three-point loading test fixture. The loading fixture consisted of a 0.317-cm (⅛-in.) radius for the nose and supports and a 1.27-cm (0.500-in.) test span. The sketch below is a schematic of the loading arrangement.

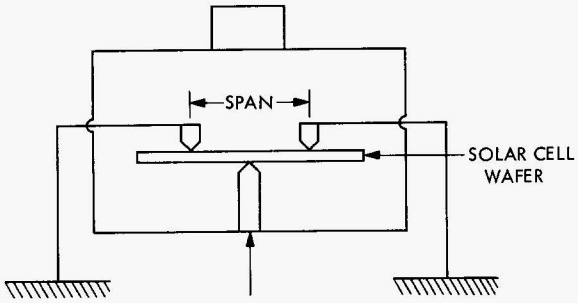

Prior to actual mechanical tests, which were performed in accordance with Federal Test Standard 406, Method 1031, the necessary dimension measurements were made for width and thickness of each silicon wafer specimen. The test parameters selected were as follows: wafer span = 1.27 cm (0.500 in.); chart speed = 50.8 and 127 cm/min; crosshead speed = 0.0508 cm/min. The general procedure employed with each set of 6–10 wafers representative of a particular processing or type of material was to test half of the specimens with one surface in contact with the center support (nose). Then the remaining specimens were tested with the opposite surface in contact with the nose. The reported results indicate whether the outermost fibers of the polished surface of the wafer are stressed either in tension or compression. The raw data obtained from these tests included load-deflection curves to failure and breaking force. From this data, analyses were made to determine the maximum failure stress and the elastic modulus in flexure. The calculations employed the following considerations from elastic-beam theory.

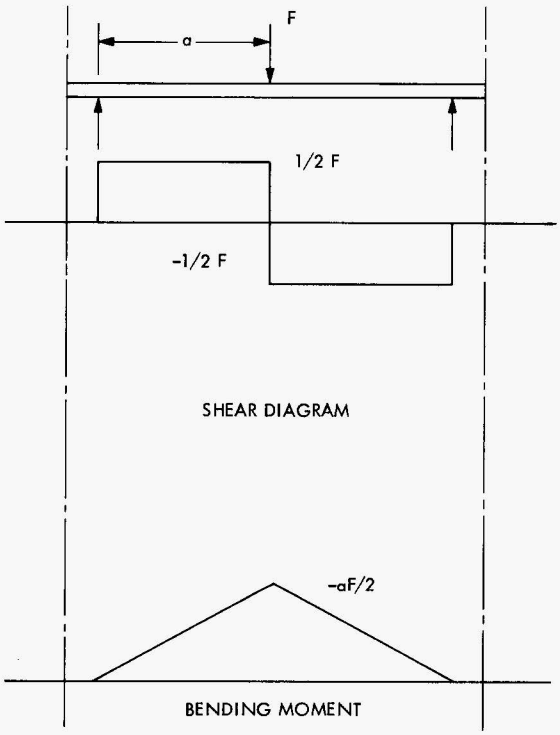

The maximum failure stress in flexure is calculated thus:

$$\sigma^* = \frac{M_y}{I}$$

$$= \frac{M^* t \times 12}{2\, bt^3}$$

or

$$\sigma^* = \frac{6\, M^*}{bt^2}$$

since $M^* = aF/2$. Then

$$\sigma^* = \frac{3aF}{bt^2}$$

where

a = half the distance between the dual test heads

b = width of the solar cell

F = breaking force

t = thickness of the solar cell

The elastic modulus may be calculated considering the cell as a cantilever beam as shown in the following sketch:

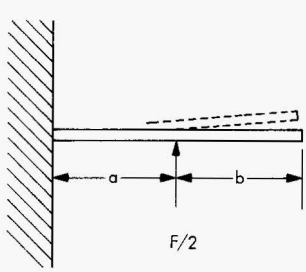

The deflection

$$(\delta_A) = \frac{1}{6}\,\frac{W}{EI}\,(2a^3) = \frac{1}{3}\,\frac{Wa^3}{EI}$$

where

$$W = F/2$$

$$\delta = \frac{Fa^3}{6\, EI}$$

and

$$I = \frac{1}{12}\, bt^3$$

Substituting and transposing, we obtain

$$\delta = \frac{2\, Fa^3}{Ebt^3}$$

and

$$E = \frac{2\, Fa^3}{\delta bt^3}$$

In determining the values for E, deflections and loads were taken at points on the curves where load vs deflection appeared most linear. Averages were calculated from either sets of three values or sets of five values. The failure stress and elastic modulus values were then given as averages (arithmetic means) in the reported results.

Appendix B

Test Procedures for Linear Thermal Expansion Tests

Measurements were made using a modified Leitz dilatometer. In this apparatus, the specimen is contacted at each end and supported by concentric fused silica tubes. The relative length is indicated by relative positions of the tubes. Movement of one with respect to the other causes movement of a prism, which results in vertical deflection of a light beam projected on a ground glass plate. Specimen length changes are magnified by a factor as large as 800. Horizontal deflection of the light beam is controlled by a thermocouple mounted between the specimen and the quartz tube.

The specimen is maintained in a dry helium atmosphere. Temperature of the specimen is varied by varying the power setting of the furnace. The furnace operates in a LN_2 environment and has a range of -196 to $+200°C$.

Power changes necessary to provide the desired temperature change are made, and the specimen is permitted to come to thermal and structural equilibrium. In this investigation, changes of approximately 50°C were made in approximately 10–20 min. When equilibrium is reached, vertical displacement of the light beam and specimen temperature are recorded, and the power is set for the next desired temperature. Displacement is hand-marked on the glass plate.

At the conclusion of a run, the specimen displacement data is read using a traveling telescope, converted to $\Delta L/L$ with respect to the original reference length at ambient temperature, and plotted as a function of temperature.

The apparatus is calibrated routinely in two steps. The magnification factor is first computed by deflecting the system with a precision micrometer. Errors due to temperature gradients within the dilatometer are then determined by analyzing the results of measurements made on a standard quartz specimen calibrated by NBS.

For maximum accuracy, the apparatus requires a 2-h stabilization period after the LN_2 environment is established in the low-temperature furnace. Considerable skill in recording and reading raw data is also required to maintain high accuracy. Under the best conditions, an uncertainty of less than $\pm 0.07 \times 10^{-4}$ $\Delta L/L$ can be maintained. This is, for example, a coefficient of uncertainty of $\pm 0.017 \times 10^{-6}$ $\Delta L/L/°C$ over 400°C. Approximately one-half of this figure is due to uncertainties in the data for the quartz standard.

Appendix C

Micro-VCM Outgassing Data on Polymeric Materials

The loss of matter by outgassing and by evaporation or sublimation is one of the most obvious effects of a thermal–vacuum environment on polymers. Because gross loss of material generally implies that the properties of polymers are altered or that test chambers and spacecraft components will be contaminated by the evaporated substances, polymers which are considered suitable for spacecraft usage are those which in laboratory tests (1) exhibit a minimum weight loss when exposed to the simulated conditions of the vacuum and thermal environment of space and (2) are found to contain a minimum of materials that vaporize at an elevated temperature in a vacuum and deposit on adjacent, cooler surfaces. The former is expressed as total weight loss; the latter is expressed as volatile condensible materials (VCM).

Outgassing properties of polymeric materials are determined at JPL by micro-VCM testing. This should not be confused with macro-VCM testing which determines the *rate* of outgassing and condensibles. Macro-VCM exposes polymeric materials at an elevated temperature in a vacuum for six weeks. Curves of outgassed weight loss and weight condensed vs time are generated. Micro-VCM determines in a 24-h period the *total* outgassing and condensibles. The key to micro-VCM testing is the comminution of the sample to expose a very large surface area to volume of material. Thus, in theory, the end point of a six-week (or infinite time) macro-VCM test can be attained in a short period of time. With the micro-VCM test, a rate value is not obtained.

The JPL micro-VCM testing is conducted at 125°C (257°F) for 24 h in a 10^{-6} torr vacuum. The VCM plates are held at 25°C (77°F). Since electronic assemblies, associated components, and other components employing polymeric materials are protected or shielded from as many hazards as possible in space flights, the above conditions simulate the extremes of those expected in actual usage.

The degree of acceptability of outgassing properties will depend on the type of material, its usage, and the location within the spacecraft. Materials used in the vicinity of optical or electronic components must meet much more rigid outgassing requirements than those used in more remote areas. The degradation of the material properties due to outgassing depends upon the type of material. The amount of degradation tolerable depends on the material usage.

NASA — JPL — Coml., L.A., Calif.